Wrinkled-up Nanochannel Networks: Long-Range Ordering, Scalability, and X-ray Investigation

Angelo Malachias,[†] Yongfeng Mei,[‡,*] Ratna K. Annabattula,[§] Christoph Deneke,[‡] Patrick R. Onck,[§] and Oliver G. Schmidt[†,‡]

[†]Max-Planck-Institut für Festkörperforschung, Heisenbergstr. 1, D-70569 Stuttgart, Germany, [‡]Institute for Integrative Nanosciences, IFW Dresden, Helmholtzstr. 20, D-01069 Dresden, Germany, and [§]Zernike Institute for Advanced Materials, University of Groningen, Nijenborgh 4, 9747 AG Groningen, The Netherlands

ABSTRACT Highly ordered two-dimensional self-organized nanochannel networks as well as free-standing nanomembranes are produced on rigid substrates by means of III—V semiconductor compressively strained layers grown on top of an etchant-sensitive material. The releasing process is controlled by regularly spaced pits obtained from photolithography and a subsequent wet chemical etching. By tuning basic film parameters such as strain and thickness, one obtains periodic arrays of two-dimensional nanochannel networks with symmetries defined by the shape and periodicity of the photolithographic starting pits. Such nanochannel networks with a submicroscale lateral feature size exhibit a surprising flexibility with respect to the crystal lattice symmetry, retaining the original film crystalline quality as confirmed by X-ray grazing-incidence diffraction (GID) measurements. Finite element modeling helps in understanding the particular process of the cross-nanochannel formation.

KEYWORDS: nanomembranes · wrinkles · nanochannels · photolithography · layer releasing · strain · long-range ordering

Self-organized channel systems at the micro- and nanometer scale are strong candidates for integrating optical, electronic, and fluidic devices, or their combinations on a single chip, that is, laboratory-on-a-chip related applications.[1–5] The research in this field has been performed mostly using polymeric materials which exhibit low production costs and suitable elastic properties.[6–8] However, despite of the inherent advantages in production, the integration of such materials with semiconductors and metals for the engineering of electronic devices involves processing steps which are often highly demanding.[9] Hence it is crucial to realize smart methods that allow for manufacturing nanofluidic devices directly on semiconductor materials.[10,11]

Recently, it has been shown that semiconductor nanochannel networks can be created by the release and bond-back of layers,[12] which can be briefly described as follows. First, an etchant-sensitive layer is grown as a sacrificial layer on a rigid substrate. A compressively strained semiconductor film is then deposited on top of the first layer. Finally, the top film is released by selective chemical etching of the first layer, allowing for the release of its internal strains after which the film bonds back to the substrate, producing wrinkles in the top surface. In the resulting morphology, the self-assembled wrinkles constitute semiconductor micro- or nanochannels with high crystalline quality, which maintain a small residual stress due to the bond-back effect.[13]

In this work, we show how micro/nanochannels can be self-organized in two dimensions by combining a simple optical lithography technique and the elastic relaxation of prestressed III—V semiconductor heteroepitaxial nanomembranes together with a wet chemical etching of a sacrificial layer. We prove the possibility of creating long-range ordered patterns over a large area by fine-tuning the size and periodicity of predefined pits. Additionally, the complete releasing of the same film into a free-standing nanomembrane that can be transferred to another substrate is developed. The strain status and crystalline quality of the obtained free-standing layers is compared to wrinkled nanomembranes by X-ray grazing-incidence diffraction (GID) measurements.

RESULTS AND DISCUSSION

For our studies, 20 and 10 nm thick $In_{0.2}Ga_{0.8}As$ films were grown on top of 80 nm AlAs layers (HF etchant-sensitive) on GaAs(001) substrates. The heteroepitaxy of the $In_{0.2}Ga_{0.8}As$ alloy on top of a GaAs lattice leads to a well-defined in-plane strain of 1.4%. This nominal strain was independently corroborated by coplanar X-ray diffraction measurements (not shown). The principle of fabrication of ordered channels is depicted in Figure 1a. Initially, optical lithography is performed to create a regular

Ⓦ This paper contains enhanced objects available on the Internet at http://pubs.acs.org/journals/ancac3.

*Address correspondence to y.mei@ifw-dresden.de.

Received for review May 20, 2008 and accepted June 30, 2008.

Published online July 18, 2008.
10.1021/nn800308p CCC: $40.75

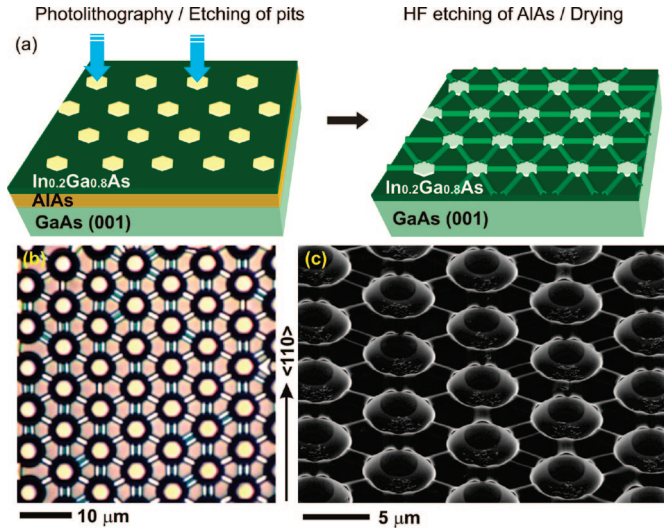

Figure 1. (a) Sketch of the steps for the fabrication of ordered channel networks. (b) Optical microscopy image of a hexagonally ordered network of channels formed from a 20 nm thick $In_{0.2}Ga_{0.8}As$ film. The hexagonal pits have 3 μm lateral size and are regularly spaced by 8 μm. (c) Scanning electron microscope image of the same network.

pattern of micrometer-sized hexagons or squares. Using a solution of HBr (50 vol %)/$K_2Cr_2O_7$ (0.5 mol/L)/CH_3COOH (100 vol %) (2:1:1),[14] deep vertical pits (trenches) are formed at the defined positions (Figure 1a). The AlAs sacrificial layer is then etched away by a HF (50 vol %)/H_2O (1:800) solution with an etching rate of approximately 1 μm/min, which releases the upper layer and allows it to relax elastically. In order to probe the crystalline quality and in-plane strain of networks and membranes, grazing-incidence diffraction (GID) measurements were also performed. The experiments were carried out in a 4 + 2 circle diffractometer at the MPI-MF beamline at ANKA. The setup used was optimized for higher photon flux at $E = 10$ keV, at the expense of angular resolution (*i.e.*, large divergence).

For a set of lithographic pit distances and growth parameters such as the AlAs/$In_xGa_{(1-x)}As$ layer thickness and In concentration x, which changes the in-plane strain, regular arrangements of channels are produced with a controlled periodicity and narrow size distribution. The optical micrograph of Figure 1b shows an ordered channel network obtained from a released 20 nm thick $In_{0.2}Ga_{0.8}As$ film with a hexagonal pit pattern. The hexagonal pits have an edge length of 3 μm and are regularly spaced with a periodicity of 8 μm, producing channels with 750 nm lateral size and 120 nm height. The scanning electron microscopy (SEM) image of Figure 1c confirms the excellent size and shape uniformity of the channels. It is noticeable that the hexagon corners are rounded off because of partial lateral etching in the HBr/$K_2Cr_2O_7$/CH_3COOH solution.[14]

In order to explore the experimental possibilities of producing different network geometries, an optical lithography mask was designed containing several 100 μm × 100 μm templates with square and hexagonal pit shapes arranged into 4- and 6-fold pattern symmetries, respectively. For the results shown here, the network template field edges were aligned along the [110] GaAs direction. In such process, the edges of all square pits are parallel to the GaAs [110] direction. Following the same alignment for the hexagonal fields results in one family of edges always parallel to the GaAs [110] as shown in Figure 1b,c. Networks fabricated with the same template field edges aligned along the [100] direction were also made and exhibited similar resulting morphologies. Apart from shape and pattern, other parameters such as pit size (w) and periodicity (l) were varied systematically from $w = 1$ to 4 μm and from $l = 3$ to 9 μm. Figure 2a summarizes graphically the configuration space range that was investigated for square and hexagonal networks. The results shown for the $In_{0.2}Ga_{0.6}As$ layers comprise 8 samples with 10 nm thick film and 10 samples with 20 nm thick film. An indicator of the network quality is represented by the size and aspect of the colored circles in the diagram. A given network is considered as "completely ordered" when all pits are connected by one or more direct channels. In a "mostly ordered" network, less than one-fourth of channel links are missing, broken, or connecting more than one pit. For "poorly ordered networks", networks with up to 50% missing or damaged channels are counted. Missing points in the diagram denote configurations that lead to completely disordered channels or are geometrically forbidden (*e.g.*, size of starting window larger than periodicity).

From the diagram, we derive that square networks exhibit a better quality for large w and relatively small l, suggesting that a short channel length is preferred for the 4-fold network symmetry. The best ordering for the hexagonal networks was found at intermediate w values and large l, indicating the formation of relatively long channels. Two paths through the configuration diagram represented by the arrows labeled A and B were chosen to depict the wrinkling behavior under different w and l conditions. Optical images of the network fields along these paths are shown in Figure 2b. The A path goes along w values of square networks spanning from $w = 1$ to 4 μm with a fixed $l = 5$ μm. For the 20 nm film, one observes that the networks evolve from a completely random channel configuration at $w = 1$ μm to a mostly ordered condition at $w = 4$ μm, with individual channels connecting the adjacent pits. The scenario is more complex for the 10 nm film. At $w = 1$ μm, one observes a multidirectional wrinkling with a clear tendency to develop channels in the [100] diagonal direction. For $w = 2$ μm, the [100] crossed channel type dominates the ordering process and a completely ordered network is obtained. For $w = 3$ μm, direct [110] channels are the preferential interpit connection with reminiscent 45° channels at some pit corners. Finally, for $w = 4$ μm, all pits are connected by

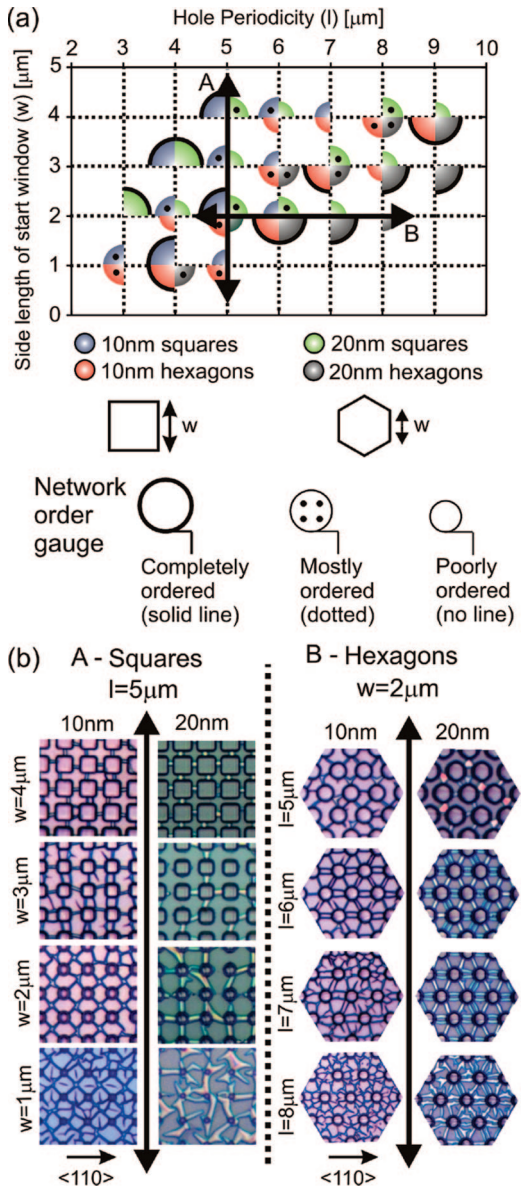

Figure 2. (a) Graphical representation of the configuration space range tested for obtaining square and hexagonally ordered networks in 10 and 20 nm thick $In_{0.2}Ga_{0.8}As$ films. A semiquantitative gauge is used to index the obtained network order. The pit edge width defined here is shown for each shape. (b) Optical images of the obtained channel patterns for two paths along the configuration space are shown for fixed hole periodicity squares—arrow A—and fixed start window size hexagons—arrow B.

direct [110] channels that are formed in the square edges.

The evolution of the ordering in hexagonal networks along the B arrow path is also shown in detail in Figure 2b. For this path, *w* is fixed to 2 μm and *l* is varied from 5 to 8 μm. Both 10 and 20 nm thick films exhibit their best ordering for $l = 6$ μm, most remarkably for the thicker film. In the hexagonal networks, longer channel distances are easily obtained as a result of the larger channel density, which is tied to the availability of pit edges and the possibility of multichannel creation. As observed in Figure 1b,c and in the right panel of Figure 2b, multichannels are dominant in the direction which is parallel to a ξ edge of the lithographic pattern template. In the other directions, oriented at ±60°, the formation of both single and multiple channels is observed. Such fact can be explained by the in-plane relaxation constraint imposed by the lithographic template edges. Since these templates comprise a square area of 100 μm × 100 μm dimensions (with edges along ξ directions), there is a limited lateral extent for the bonding-back of the released film. The group of channels aligned along the [110] edge must accommodate all the additional surface area which is obtained along this direction after the layer is released, therefore giving rise to a large number of multiple channels. The released surface area comprised between the [1 −1 0] template edges can be accommodated in both +60° or −60° channel families. Due to this larger site availability, single channels are dominant in these tilted directions. Finally, connections between pits for this 6-fold symmetry are always observed between edges with no formation of corner-to-corner channels as seen in the 4-fold structures. The reduced presence of this effect may be related to the larger corner angle in the hexagons.

The channel density and, consequently, the average channel-to-channel periodicity observed in Figure 1b,c and Figure 2b can be tuned by a few parameters of intrinsic and extrinsic nature. Intrinsically, the wrinkling periodicity is affected by the film thickness as well as by the in-plane strain. As shown in a previous study,[12] the total surface area of a released film corresponds to the equivalent area for a relaxed film. Hence, reducing the strain produces a lower density of wrinkles and therefore an increase in the channel periodicity. The role of the film thickness is tied to the strain gradient produced between the upper and lower film interfaces.[15] For a fixed strain, a thinner film is more susceptible to accept pronounced bowings and will produce channels which are laterally smaller. Therefore, due to the criterion of the total area discussed above, the channel density will be larger. Despite of the intrinsic parameters, the periodicity is also affected by extrinsic parameters which are related to the processing and under-etching such as the shape and size of the starting pits, ultimately related to the length of

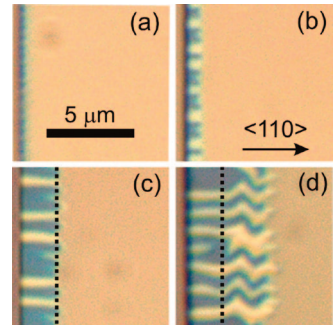

Figure 3. Optical microscope images of AlAs under-etch time evolution for the 20 nm $In_{0.2}Ga_{0.8}As$ film through a long trench edge. The images correspond to etching times of (a) 1 min, (b) 2 min, (c) 3 min, and (d) 6 min.

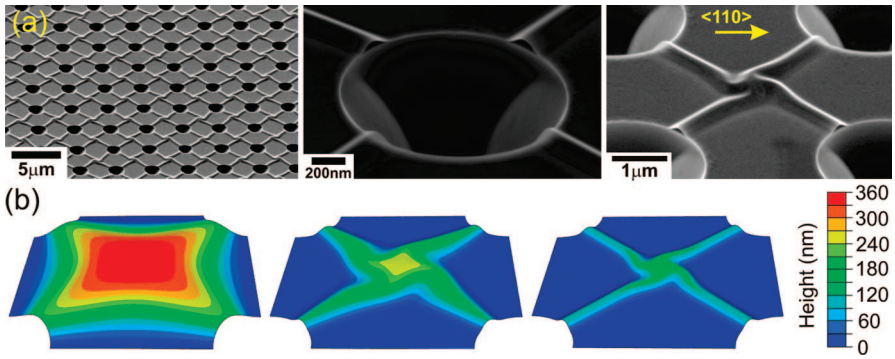

Figure 4. (a) SEM images of crossed channels in $w = 1$ μm, $l = 4$ μm configuration. (b) Selected snapshots from the FEM simulation of the buckling and draping down process that leads to the formation of crossed channels.

Ⓦ Animated computations of top and lateral visions of the buckling and draping down process that leads to the formation of crossed-channels of panel b are provided.

the etching front. As shown in ref 12, wrinkling in isolated micrometer-sized pits consists of a shape-dependent process driven by the existence of predefined corners. In small pit sizes, the formation of channels may be favorable on corners, which would be a region for the confluence of film relaxation in more than one in-plane direction. As the side length of pits becomes larger, channels formed on corners become less important for the local film relaxation relatively to channels formed at the pit edges. By extrapolating the edge length toward an infinitely long trench, the periodicity would converge to a fixed equilibrium value. Since the interplay of corner-edge extrinsic effects and intrinsic parameters involve a relatively large number of degrees of freedom, a preliminary lithographic step that spans over several network configurations is needed to probe the feasibility of a given semiconductor channel network, as employed here (Figure 2a). In such an approach, it is possible to fix a desired set of parameters (*e.g.*, the extrinsic ones) and test different sets of the intrinsic parameters by, for example, varying the layer thickness and/or strain.

Besides the interplay between intrinsic and extrinsic parameters, the formation of ordered networks is also limited by other constraints related with the etching process. Perhaps the most evident limitation which can be experimentally observed is the maximum straight channel length. Figure 3a−d shows optical microscope images of the channel formation and evolution dependence with AlAs under-etching time and the wrinkling process along a [110] oriented steep edge in the 20 nm $In_{0.2}Ga_{0.8}As$ film. For etching times shorter than 1 min, some wiggles are observed at the border of the film (Figure 3a). As the AlAs under-etching proceeds, the initial wiggles evolve into well-defined straight channels up to a limited critical length l_c of ~2 μm (Figure 3b,c). For etching times larger than 3 min in our experimental conditions, the channels no longer evolve straight but exhibit a zigzag morphology and a multidirectional relaxation behavior as shown in Figure 3d. These effects are most probably a consequence of wrinkling in the under-etching direction, perpendicular to the edge (trench). As the film bonds-back in the regions close to the initial pit (trench), it creates tie points which do not allow for lateral in-plane motion. This restriction induces an irregular buckling of the film after a given critical length, leading to the observed zigzag configuration. Hence, it can be suggested for our samples that the successful formation of ordered networks with straight direct channels connecting pits is constrained by the channel length that is equal or smaller than $2l_c$. For the square networks, this condition can be represented as $l - w \leq 4$ μm, while for the hexagonal networks, the pit arrangement leads to $l - \sqrt{3}w \leq 4$ μm. HF concentration is another important and extrinsic factor in our experiments, which will strongly influence our wrinkled structures because of the dynamics of wet chemical etching and the bond-back effect.[12] In this work, the HF dilution was optimized to produce an etching rate which is, on one hand, slow enough to allow a uniform elastic energy relaxation of the prestressed layer and generate homogeneous channels but, on the other hand, efficient enough to remove all of the sacrificial layer and leave a clean and bondable interface between substrate and the prestressed layer.

A special network with crossed-nanochannels was found to form in the 10 nm film with square pits for the $w = 2$ μm; $l = 5$ μm condition, shown in Figure 2b, as well as for $w = 1$ μm; $l = 4$ μm, shown in the SEM images of Figure 4a. In such cases, the small initial squares used for lithographic patterning are near the limit of the resolution for our optical lithography. Rounded starting pits are then obtained as a result of limited resolution. The competition between corners and edges as favorable channel nucleation sites in these pits may be reduced or suppressed and channels are formed along the 45° [100] direction. Such effect may be triggered by the anisotropic elasticity of the crystal or the anisotropic HF etching of AlAs, being slightly faster in the [100] direction.[16] Due to the lack of well-defined edges and corners, the pits are then connected by crossed channels. The magnification in the rightmost panel of Figure 4a shows that these channels are arranged into single nondefective 4-fold structures. An explanation for the particular shape of the channel network might originate from general buckling mechanisms as reported previously for polymeric systems.[17] Finite element method (FEM) simulations shown in Figure 4b describe the process of cross-channel formation. Boundary conditions are applied such as to reflect the symmetry of the square 4-fold symmetry. When the film is released from the substrate by the etching process, the film can release its internal strains

by buckling up, forming a dome that has a maximum height (red color) in the center, as shown in the first (left) snapshot of Figure 4b. At this stage, the under-etch is complete, and upon drying, the film starts to bond back from tie points at which lateral in-plane motion is constrained. The attractive (cohesive) forces between film and substrate during drying initially supply sufficient energy to bond back the film, thereby storing strain energy in the film. During this stage, the deformation mode in the film switches from a symmetric to an asymmetric, lower-energy configuration, as shown in the second (middle) snapshot. The final network configuration is formed (see right, last, snapshot of Figure 4b) when the energy gained in creating new film−substrate contact is balanced by the strain energy needed to deform the film further into a tighter bend. The typical rotational incompatibility at the center is a characteristic feature of the crossed-channel networks (see Figure 4a, left and right panels), which has also been observed in polymeric systems.[17] Animations of the computations under different views are supplied as Web enhanced objects.

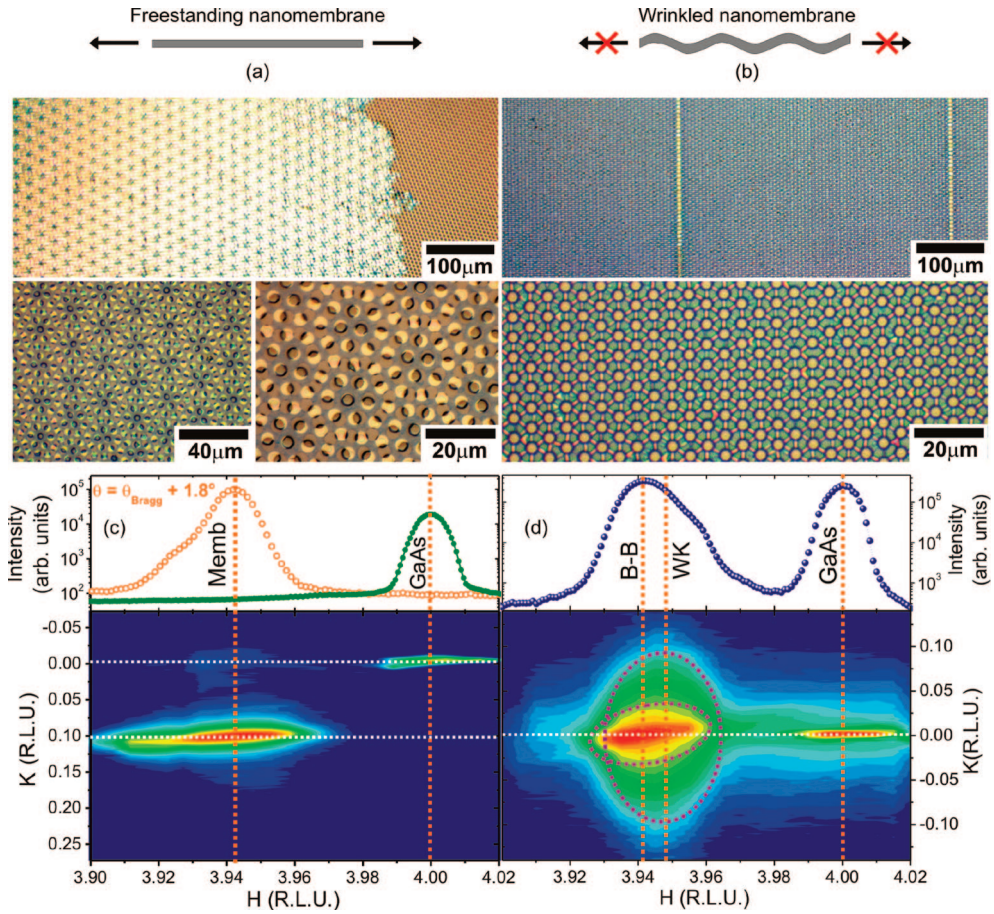

Figure 5. (a) Optical images of a free-standing 20 nm thick $In_{0.2}Ga_{0.8}As$ nanomembrane obtained from a hexagonal ($w = 2$ μm, $l = 6$ μm) patterned in a 5 mm^2 sample. The membrane is totally released in liquid and subsequently transferred to its original substrate. (b) A 5 mm^2 wrinkled network obtained for similar conditions. In this case, the film is held to the substrate by the evaporation of long 8 nm thick Cr stripes with 10 μm lateral width. Panels (c) and (d) show X-ray diffraction measurements in the vicinity of the GaAs (400) reflection (see text).

Since desired applications for both wrinkled micro-nanochannel networks and free-standing nanomembranes may require high crystalline quality, it is worth evaluating structural properties such as strain and domain sizes by X-ray diffraction. The complete release of a semiconductor film from its host substrate has been shown before[18,19] and follows etching procedures similar to those discussed above. Figure 5a shows optical microscopy images of a completely released 20 nm thick $In_{0.2}Ga_{0.8}As$ film which was transferred back to its original GaAs substrate. For releasing this membrane, a hexagonal network pattern of pits with $w = 2$ μm and $l = 6$ μm is lithographically defined over a 5 mm^2 sample. After the etching of pits and HF under-etching of the AlAs layer, the sample is immediately dipped in deionized water. Due to the lack of unetched AlAs regions and the absence of large bond-back regions in wet conditions, the film is, after a gentle agitation, released completely and floats on the surface of the water vessel. It can then be picked up by a new desired substrate. The nanomembrane shown in Figure 5a was transferred back to the initial GaAs substrate in which the original pits are recognized in the optical image as the structures surrounded by black boundaries. For the light contrast used, the nanomembrane material is seen in blue (bond back) and white (pit covering) colors. A careful inspection in the optical microscope reveals that the membrane is flat.

In order to obtain large wrinkled networks and avoid the formation of a free-standing membrane, an additional lithographic step must be performed to fix the nanomembrane on the substrate. We have chosen a simple approach that consists of the thermal evaporation of long chromium stripes which are resistant to the etching of pits. These stripes are a few millimeters long and have a 10 μm lateral size. The thickness of the Cr stripes used here is 6 nm with a lateral periodicity of 300 μm. As shown in the optical microscopy image of Figure 5b, a completely ordered network is obtained for the $w = 2$ μm, $l = 6$ μm condition.

X-ray grazing-incidence diffraction (GID) θ−2θ scans and reciprocal space maps were measured in the vicin-

ity of the GaAs (400) position for both the free-standing membrane and wrinkled hexagonal network. Measurements in GID geometry are sensitive to the lattice parameter parallel to the surface, and hence the existence of biaxial in-plane strain can be probed. The results are shown in Figure 5c,d, respectively. A $\theta-2\theta$ longitudinal scan on the membrane sample is shown by the solid green dots in Figure 5c. Only the GaAs (400) peak is observed in this scan, revealing that the lattices from substrate and released film are no longer aligned. In order to find out the (400) diffraction from the membrane, the 2θ angle is fixed at the relaxed $In_{0.2}Ga_{0.8}As$ reciprocal space position ($h = 3.942$), and the sample angle is rotated until an intensity peak is measured. In this case, the membrane peak is observed in a relative angular displacement of 1.8°. The 4-fold symmetry of this reflection was checked for the film by rotating the sample by more than 180°, proving that the diffraction comes from one single large two-dimensional crystal. The difference in the crystalline registry is better seen in the intensity map of Figure 5c. As shown in the map, the membrane peak is centered in the relaxed film reciprocal space position in *h* and has a narrow profile along the transversal (*k*) direction, indicating the large lateral size of the crystalline domain in the released film. A weak diffracted intensity is also observed at lower *h* values and can be attributed to stretched regions of the membrane with a residual tensile strain of 0.35%. A lateral size of 0.79(5) μm and a very small average mosaic spread of 0.12(1)° were obtained from the analysis of the θ transversal scans (rocking curves) that constitute the *hk* map as well as from similar measurements in other reflections.[20]

The same set of measurements was performed on the hexagonal network of Figure 5b. From the longitudinal $\theta-2\theta$ scan, one observes that besides the GaAs peak a broad intensity distribution is found spanning from the $h \sim 3.93$ to $h \sim 3.96$. Although the origin of this scattering cannot be inferred from this single scan, it indicates that the lattice of the wrinkled film is aligned with the lattice of the substrate. The reciprocal space map of Figure 5d provides clearer evidence of the origin of the diffraction from the film. Two main components are identified and marked by the dashed ellipses. The first component is narrow in the *k* direction and centered at the fully relaxed film position in *h*. Such scattering is related to large flattened real space structures with average zero strain and may be therefore assigned to the bond-back areas.[13,19] The second component is much broader in the transversal *k* direction and centered in a slightly larger *h* value. These characteristics indicate that the broad component is originated by smaller real space crystalline regions with an average compressive strain that spans from 0.2 to 0.45%. Such a broad component is most likely related to the channels. For the curved surface of wrinkles, the effective scattering cross-section is expected to correspond mostly to flattened regions parallel to the substrate plane such as the channel apex and bottom. This interpretation is supported by the systematic smearing out of the second component observed for high index in-plane reflections such as (440), (620), and (800) that have an enhanced sensibility to crystalline disorientation. From the analysis of the transversal scans, lateral sizes of 0.13(2) μm and 50(5) nm were obtained for the bond-back and channel scattering cross section. The smaller lateral size of the bond-back regions in relation to the free-standing membrane may indicate that this part of the film has a larger effective out-of-plane layer misalignment as a result from the wrinkling process. An average mosaic spread of 0.14(1)° was found for the bond-back regions and confirms that an excellent, similar crystalline quality is obtained for the wrinkled and the fully released nanomembranes.

CONCLUSIONS

In summary, we have demonstrated how long-range ordered nanochannel networks can be obtained from flat strained semiconductor films on rigid substrates by using a conventional photolithography. Such patterns can be also used as templates for organizing light-emitting strained structures,[13] polymer films, small cells, or soft-magnetic materials. Different symmetries were experimentally explored to clarify the formation principle, and the formation mechanism of crossed channels was depicted from FEM calculations. X-ray diffraction measurements were able to access the crystalline quality of wrinkled and fully released nanomembranes. From the material properties and results shown here, we expect that this technique can be employed to integrate semiconductor optoeletronic properties and nanofluidic capabilities[12] for novel laboratory-on-a-chip applications. The complete releasing of direct band gap III−V nanomembranes with the possibility of transferring to any substrate opens new opportunities for possible novel applications.[21]

METHODS

Film Growth, Network Reproducibility. The III−V semiconductor layers were grown on GaAs (001) substrates in a RIBER-32 MBE system. After the growth of a 500 nm GaAs buffer, 80 nm AlAs and 10 nm/20 nm $In_{0.2}Ga_{0.8}As$ were deposited. The crystalline quality and absence of structural defects (such as dislocations) in these layers were checked by means of coplanar X-ray diffraction in a 4-circle Bruker-AXS system and grazing-incidence diffraction at ANKA. Several samples were lithographically patterned to probe the reproducibility of channel network formation, comprising 8 samples for the 10 nm thick $In_{0.2}Ga_{0.8}As$ film and 10 samples for the 20 nm thick $In_{0.2}Ga_{0.8}As$ film. Additionally, since the total area needed for probing the complete parameter space depicted in Figure 2 for each shape was about 1.2 mm × 1.2 mm, each sample of 5−6 mm lateral size con-

tained 4−5 fields of square-shaped networks and 4−5 fields of hexagonal networks. Therefore, in total, more than 40 fields of each *w*−*l* combination were tested for each film thickness and network geometry, assuring the process repeatability. For the results shown here, the network template field edges were aligned along the [110] GaAs direction. Networks fabricated with the same template field edges aligned along the [100] direction were also made and exhibited similar resulting morphologies.

Synchrotron Grazing-Incidence X-ray Diffraction. Surface-sensitive diffraction experiments in grazing-incidence geometry were carried out in a 4 + 2 circle diffractometer at the MPI-MF beamline at ANKA. The setup used was optimized for higher photon flux at $E = 10$ keV, at the expense of angular resolution (*i.e.*, large divergence). For the calculation of sizes from our X-ray measurements, the instrumental broadening is evaluated by measurements performed in our MBE-grown single crystal flat films. The width of a measured peak δ_{meas} is then related to a deconvoluted width δ_{real} by $\delta_{meas}^2 \equiv \delta_{real}^2 \pm \delta_{inst}^2$, where δ_{inst} is the instrumental resolution. A set of five in-plane reflections were measured for the extraction of mosaic spread values:[20] (220), (400), (440), (620), and (800).

HF Etching Solution Risks and Caution Procedures. Only work in a closed system or under a functional chemical hood with the safety window as closed as possible. Avoid all contact with hydrofluoric acid at all times.

Acknowledgment. This work was supported by the BMBF (03X5518) and MicroNed programme (FUNMOD cluster, project 4-C-4). The authors would like to thank A. Stierle, S. Doyle, and R. Weigel for the support in the X-ray measurements at the MPI-MF beamline (ANKA), and E. Coric for the SEM images.

REFERENCES AND NOTES

1. Thorsen, T.; Maerkl, S. J.; Quake, S. R. Microfluidic Large-Scale Integration. *Science* **2002**, *298*, 580–584.
2. Hong, J. W.; Quake, S. R. Integrated Nanoliter Systems. *Nat. Biotechnol.* **2003**, *21*, 1179–1183.
3. Wolfe, D. B.; Conroy, R. S.; Garstecki, P.; Mayers, B. T.; Fischbach, M. A.; Paul, K. E.; Prentiss, M.; Whitesides, G. M. Dynamic Control of Liquid-Core/Liquid-Cladding Optical Waveguides. *Proc. Natl. Acad. Sci. U.S.A.* **2004**, *101*, 12434–12438.
4. Gunther, A.; Jhunjhunwala, M.; Thalmann, M.; Schmidt, M. A.; Jensen, K. F. Micromixing of Miscible Liquids in Segmented Gas-Liquid Flow. *Langmuir* **2005**, *21*, 1547–1555.
5. Squires, T. M.; Quake, S. R. Microfluidics: Fluid Physics at the Nanoliter Scale. *Rev. Mod. Phys.* **2005**, *77*, 977–1026.
6. Huh, D.; Mills, K. L.; Zhu, X.; Burns, M. A.; Thouless, M. D.; Takayama, S. Tuneable Elastomeric Nanochannels for Nanofluidic Manipulation. *Nat. Mater.* **2007**, *6*, 424–428.
7. Yoo, P. J.; Lee, H. H. Evolution of a Stress-Driven Pattern in Thin Bilayer Films: Spinodal Wrinkling. *Phys. Rev. Lett.* **2003**, *91*, 154502.
8. Yoo, P. J.; Suh, K. Y.; Lee, H. H. Polymer Elasticity-Driven Wrinkling and Coarsening in High Temperature Buckling of Metal-Capped Polymer Thin Films. *Phys. Rev. Lett.* **2004**, *93*, 034301.
9. Wang, L.; Yoon, M.-H.; Lu, G.; Yang, Y.; Facchetti, A.; Marks, T. J. High-Performance Transparent Inorganic—Organic Hybrid Thin-Film n-type Transistors. *Nat. Mater.* **2006**, *5*, 893–900.
10. Psaltis, D.; Quake, S. R.; Yang, C. Developing Optofluidic Technology through the Fusion of Microfluidics and Optics. *Nature* **2006**, *442*, 381–386.
11. Schmidt, O. G.; Schmarje, N.; Deneke, C.; Müller, C.; Jin-Phillipp, N.-Y. Three-Dimensional Nano-Objects Evolving from a Two-Dimensional Layer Technology. *Adv. Mater.* **2001**, *13*, 756–759.
12. Mei, Y. F.; Thurmer, D. J.; Cavallo, F.; Kiravittaya, S.; Schmidt, O. G. Semiconductor Sub-Micro-/Nanochannel Networks by Deterministic Layer Wrinkling. *Adv. Mater.* **2007**, *19*, 2124–2128.
13. Mei, Y. F.; Kiravittaya, S.; Benyoucef, M.; Thurmer, D. J.; Zander, T.; Deneke, Ch.; Cavallo, F.; Rastelli, A.; Schmidt, O. G. Optical Properties of a Wrinkled Nanomembrane with Embedded Quantum Well. *Nano Lett.* **2007**, *7*, 1676–1679.
14. Rastelli, A.; Ulhaq, A.; Deneke, Ch.; Wang, L.; Benyoucef, M.; Coric, E.; Winter, W.; Mendach, S.; Horton, F.; Cavallo, F. Fabrication and Characterization of Microdisk Resonators with In(Ga)As/GaAs Quantum Dots. *Phys. Status Solidi C* **2006**, *3*, 3641–3645.
15. Huang, W.-P.; Cheng, H. H.; Fedorchenko, A. I.; Wang, A.-B. Strain on Wrinkled Bilayer Thin Film. *Appl. Phys. Lett.* **2007**, *91*, 053103.
16. Lühn, O. Herstellung von A(III)-B(V)-Nanoröhren aus Epitaktischen Dünnschichtsystemem, Ph.D. Thesis; Institut für Chemie und Mineralogie, Universität Leipzig, 2004.
17. Edmondson, S.; Frieda, K.; Comrie, J. E.; Onck, P. R.; Huck, W. T. S. Buckling in Quasi-2D Polymers. *Adv. Mater.* **2006**, *18*, 724–728.
18. Sun, Y.; Rogers, J. A. Inorganic Semiconductors for Flexible Electronics. *Adv. Mater.* **2007**, *19*, 1897–1916.
19. Roberts, M. M.; Klein, L. J.; Savage, D. E.; Slinker, K. A.; Friesen, M.; Celler, G.; Eriksson, M. A.; Lagally, M. G. Elastically Relaxed Free-Standing Strained-Silicon Nanomembranes. *Nat. Mater.* **2006**, *5*, 388–393.
20. For the calculation of sizes from our X-ray measurements, the instrumental broadening is evaluated by measurements performed in our MBE-grown single crystal flat films. The width of a measured peak δ_{meas} is then related to a deconvoluted width δ_{real} by $\delta_{meas}^2 = \delta_{real}^2 + \delta_{inst}^2$, where δ_{inst} is the instrumental resolution. A set of five in-plane reflections were measured—(220), (400), (440), (620), and (800)—for the extraction of mosaic spread values. The mosaic spread values were extracted according to the method outlined by: Renaud, G.; Barbier, A.; Robach, O. Growth, Structure, and Morphology of the Pd/MgO(001) Interface: Epitaxial Site and Interfacial Distance. *Phys. Rev. B* **1999**, *60*, 5872–5882.
21. Peng, W.; Roberts, M. M.; Nordberg, E. P.; Flack, F. S.; Colavita, P. E.; Hamers, R. J.; Savage, D. E.; Lagally, M. G.; Eriksson, M. A. Single-Crystal Silicon/Silicon Dioxide Multilayer Heterostructures Based on Nanomembrane Transfer. *Appl. Phys. Lett.* **2007**, *90*, 183107.